The Astrophysical Journal, 923:149 (18pp), 2021 December 20 https://doi.org/10.3847/1538-4357/ac2e93

Measuring the Mass of the Large Magellanic Cloud with Stellar Streams Observed by S^5

Nora Shipp[1,2], Denis Erkal[3], Alex Drlica-Wagner[1,2,4], Ting S. Li[5,6,7,21], Andrew B. Pace[8], Sergey E. Koposov[9,10,11], Lara R. Cullinane[12], Gary S. Da Costa[12,13], Alexander P. Ji[1,2,6], Kyler Kuehn[14,15], Geraint F. Lewis[16], Dougal Mackey[12,13], Jeffrey D. Simpson[13,17], Zhen Wan[16], Daniel B. Zucker[18], Joss Bland-Hawthorn[13,16], Peter S. Ferguson[19,20], and Sophia Lilleengen[3]
(S^5 Collaboration)
[1] Department of Astronomy and Astrophysics, University of Chicago, Chicago IL 60637, USA; noraship@uchicago.edu
[2] Kavli Institute for Cosmological Physics, University of Chicago, Chicago, IL 60637, USA
[3] Department of Physics, University of Surrey, Guildford GU2 7XH, UK
[4] Fermi National Accelerator Laboratory, PO Box 500, Batavia, IL 60510, USA
[5] Department of Astronomy and Astrophysics, University of Toronto, 50 St. George Street, Toronto ON, M5S 3H4, Canada
[6] Observatories of the Carnegie Institution for Science, 813 Santa Barbara Street, Pasadena, CA 91101, USA
[7] Department of Astrophysical Sciences, Princeton University, Princeton, NJ 08544, USA
[8] McWilliams Center for Cosmology, Carnegie Mellon University, 5000 Forbes Avenue, Pittsburgh, PA 15213, USA
[9] Institute for Astronomy, University of Edinburgh, Royal Observatory, Blackford Hill, Edinburgh EH9 3HJ, UK
[10] Institute of Astronomy, University of Cambridge, Madingley Road, Cambridge CB3 0HA, UK
[11] Kavli Institute for Cosmology, University of Cambridge, Madingley Road, Cambridge CB3 0HA, UK
[12] Research School of Astronomy and Astrophysics, Australian National University, Canberra, ACT 2611, Australia
[13] Centre of Excellence for All-Sky Astrophysics in Three Dimensions (ASTRO 3D), Australia
[14] Lowell Observatory, 1400 W Mars Hill Road, Flagstaff, AZ 86001, USA
[15] Australian Astronomical Optics, Faculty of Science and Engineering, Macquarie University, Macquarie Park, NSW 2113, Australia
[16] Sydney Institute for Astronomy, School of Physics, A28, The University of Sydney, NSW 2006, Australia
[17] School of Physics, UNSW Sydney, NSW 2052, Australia
[18] Department of Physics & Astronomy, Macquarie University, Sydney, NSW 2109, Australia
[19] George P. and Cynthia Woods Mitchell Institute for Fundamental Physics and Astronomy, Texas A&M University, College Station, TX 77843, USA
[20] Department of Physics and Astronomy, Texas A&M University, College Station, TX 77843, USA
Received 2021 July 27; revised 2021 October 8; accepted 2021 October 8; published 2021 December 17

Abstract

Stellar streams are excellent probes of the underlying gravitational potential in which they evolve. In this work, we fit dynamical models to five streams in the Southern Galactic hemisphere, combining observations from the Southern Stellar Stream Spectroscopic Survey (S^5), Gaia EDR3, and the Dark Energy Survey, to measure the mass of the Large Magellanic Cloud (LMC). With an ensemble of streams, we find a mass of the LMC ranging from $\sim$14–19 $\times 10^{10}\,M_\odot$, probed over a range of closest approach times and distances. With the most constraining stream (Orphan–Chenab), we measure an LMC mass of $18.8^{+3.5}_{-4.0} \times 10^{10}\,M_\odot$, probed at a closest approach time of 310 Myr and a closest approach distance of 25.4 kpc. This mass is compatible with previous measurements, showing that a consistent picture is emerging of the LMC's influence on structures in the Milky Way. Using this sample of streams, we find that the LMC's effect depends on the relative orientation of the stream and LMC at their point of closest approach. To better understand this, we present a simple model based on the impulse approximation and we show that the LMC's effect depends both on the magnitude of the velocity kick imparted to the stream and the direction of this kick.

Unified Astronomy Thesaurus concepts: Milky Way Galaxy (1054); Local Group (929); Stellar streams (2166); Large Magellanic Cloud (903)

1. Introduction

The mass of the Large Magellanic Cloud (LMC), the Milky Way's largest satellite galaxy, has proven notoriously difficult to measure. Efforts to directly measure the mass of the LMC from the dynamics of its star clusters (Schommer et al. 1992) and rotation curve (van der Marel & Kallivayalil 2014) both yield relatively modest estimates of $\sim 2 \times 10^{10}\,M_\odot$ within ~ 9 kpc. More recent measurements with Gaia yield similar results (e.g., Vasiliev 2018; Cullinane et al. 2020; Wan et al. 2020a). However, several distinct lines of reasoning suggest that the LMC may have a total mass that is up to an order of magnitude larger. First, the LMC's large speed relative to the Milky Way (e.g., Kallivayalil et al. 2006) is consistent with it being on its first passage around the Milky Way (Besla et al. 2007). Given this first passage scenario and the close association of the LMC and the Small Magellanic Cloud (SMC) in both position and velocity, it is reasonable to assume that they were accreted onto the Milky Way together. In order for the SMC to have initially been gravitationally bound to the LMC, the mass of the LMC must be greater than $\sim 10^{11}\,M_\odot$ (Kallivayalil et al. 2013). Second, accounting for the LMC's effect on the *timing argument* for the Milky Way and M31, as well as the nearby Hubble flow, gives an LMC mass of $2.5 \times 10^{11}\,M_\odot$ (Peñarrubia et al. 2016). Third, *N*-body simulations of the LMC on a first-infall orbit favor a massive LMC up to $2.5 \times 10^{11}\,M_\odot$ to explain the warp in the Milky Way's H I

[21] NHFP Einstein Fellow.

disk (Weinberg 1998; Levine et al. 2006; Weinberg & Blitz 2006; Laporte et al. 2018). Finally, abundance matching based on the stellar mass of the LMC ($M_* = 2.7 \times 10^9\,M_\odot$; van der Marel et al. 2002) gives a peak halo mass of $\sim 2 \times 10^{11}\,M_\odot$ (Boylan-Kolchin et al. 2010; Behroozi et al. 2013; Moster et al. 2013; Dooley et al. 2017a, 2017b). These arguments suggest that direct dynamical tracers are only measuring the central region of a much more massive LMC halo.

Stellar streams, the remnants of recently disrupted dwarf galaxies and globular clusters, provide a direct dynamical tracer of the mass of the LMC at much larger distances. The influence of the LMC on the behavior of stellar streams around the Milky Way was first considered in detail by Law & Majewski (2010), who discussed the interaction of a relatively light LMC ($<6 \times 10^{10}\ M_\odot$) with the Sagittarius stream and found that it could have a significant effect. Following the same argument, Vera-Ciro & Helmi (2013) showed that an LMC with a mass of $8 \times 10^{10}\,M_\odot$ could change the shape of the Milky Way halo inferred by Law & Majewski (2010), making it more spherical. Along these lines, Gómez et al. (2015) found that the infall of a $1.8 \times 10^{11}\,M_\odot$ LMC would induce a significant reflex motion in the Milky Way, which would affect the Sagittarius stream.

Recently, the Dark Energy Survey (DES) discovered a large number of stellar streams in the southern hemisphere (Shipp et al. 2018). Gaia then provided unprecedented measurements of proper motions of greater than 10^9 Milky Way stars, enabling the measurement of the proper motions of the DES streams (Shipp et al. 2019). Many of these streams are close in projection to the LMC, suggesting the exciting opportunity to probe the mass of the LMC at large radii with multiple direct dynamical tracers. Such a measurement was proposed by Erkal et al. (2018), who predicted the effect of the LMC on the Tucana III (Tuc III) stream and found that the LMC could induce a substantial proper motion perpendicular to the track of the stream on the sky. They further argued that the size of this offset could be used to measure the mass of the LMC. Interestingly, the proper motion offset predicted by Erkal et al. (2018) was not observed by Shipp et al. (2019), using data from Gaia DR2 (Gaia Collaboration et al. 2018).

The next attempt to perform this measurement came when Koposov et al. (2019) used data from Gaia DR2 to determine that the Orphan stream discovered in the Sloan Digital Sky Survey (SDSS; Belokurov et al. 2006; Grillmair 2006) and the Chenab stream discovered in DES (Shipp et al. 2018) likely originated from the same progenitor. Erkal et al. (2019) proposed that the large-scale wobble of the joint Orphan–Chenab stream track, together with the misalignment between the track and proper motion reported by Koposov et al. (2019), could be best explained as a result of an interaction between the stream and the LMC. Furthermore, Erkal et al. (2019) were able to fit the track of the Orphan–Chenab stream in an aspherical Milky Way potential, including an infalling LMC, to simultaneously measure an LMC mass of $1.38^{+0.27}_{0.24} \times 10^{11}\,M_\odot$ and a Milky Way mass of $3.80^{+0.14}_{0.11} \times 10^{11}\,M_\odot$ within 50 kpc. Subsequently, Vasiliev et al. 2021 used the Sagittarius stream to simultaneously fit the LMC and Milky Way potential and obtained an LMC mass of $(1.3 \pm 0.3) \times 10^{11}\,M_\odot$.

In this paper, we extend the analyses of Erkal et al. (2018) and Erkal et al. (2019) to five of the DES streams with proper motions measured by Gaia EDR3 (Gaia Collaboration et al. 2016, 2021) and radial velocities measured by the Southern Stellar Stream Spectroscopic Survey (S^5; Li et al. 2019). In Section 2, we describe the data used in this work. In Section 3, we explain how we fit each stream. In Section 4, we present our measurement of the LMC mass from each stream. In Section 5, we discuss the implications of our results before concluding in Section 6.

2. Data

2.1. Observations

The precise modeling of stellar streams requires 6D phase-space measurements, consisting of 3D positions and 3D velocities. Until recently, such measurements were available for only a small number of streams (e.g., Majewski et al. 2004; Koposov et al. 2010; Sesar et al. 2015; Ibata et al. 2016). S^5, in conjunction with astrometric data from Gaia and photometry from DES, has provided unprecedented systematic 6D measurements of over 20 streams in the Southern Hemisphere. Here, we provide a brief overview of S^5, and we refer readers to Li et al. (2019) for more details. S^5 uses the Two-degree Field (2dF) fiber positioner (Lewis et al. 2002) coupled with the dual-arm AAOmega spectrograph (Sharp et al. 2006) on the 3.9 m Anglo-Australian Telescope (AAT). 2dF provides 392 science fibres that can be distributed across a field of view of ~ 3 deg^2. The gratings employed were 580 V on the blue arm and 1700D on the red arm, corresponding to spectral resolutions of $\sim$1300 and $\sim$10,000, respectively. The gratings were chosen to achieve the highest spectral resolution in the red centered on the near-infrared calcium triplet lines in order to derive precise radial velocities of stream members. Both radial velocities and stellar atmospheric parameters of each star were derived simultaneously using the `rvspecfit`[22] template fitting code (Koposov 2019; Li et al. 2019). For each stream field, the average exposure time is about 2 hr to reach a signal-to-noise ratio (S/N) $\sim$5 at $r = 18.5$ for radio velocity precision ~ 1 km s^{-1}.

2.2. Stream Selection

In this study, we consider the southern streams that were observed with AAT by the end of 2018. ATLAS, Chenab, Elqui, Indus, Phoenix, Jhelum, and Aliqa Uma were observed by S^5 in 2018 (Li et al. 2019), while the Tuc III stream was observed with the same setup as an S^5 pilot program (Li et al. 2018) prior to 2018. We selected five of these streams—ATLAS, Chenab, Elqui, Indus, and Phoenix, with which to fit the mass of the LMC. These streams were selected because they have complete 6D phase-space measurements, and they show no signs of significant perturbation beyond the LMC that would require additional model complexity.

We exclude three streams from our final LMC mass analysis due to evidence of clear additional perturbations. First, we exclude Aliqa Uma, which has been shown to be an extension of the ATLAS stream (Li et al. 2021a). Aliqa Uma has been separated from the ATLAS stream by an unknown perturber. Since our fits only include the potential of the Milky Way and the LMC, they are unable to reproduce such small-scale features. We also examine the streams observed by S^5 for evidence of perturbation by the Milky Way bar. We do this by including an analytic bar potential, as described in Section 5.2.1 of Li et al. (2021a). For each stream, we sample the stream orbital parameters and the bar pattern speed 100 times.

[22] https://github.com/segasai/rvspecfit

For the pattern speed, we use $\Omega = 41 \pm 3\,\mathrm{km\,s^{-1}\,kpc}$ from Sanders et al. (2019). We compare the resulting stream models by eye to the models excluding the bar, and find that of the S^5 streams, only Tuc III is likely to have been significantly perturbed by the bar. We therefore exclude the Tuc III stream from our analysis. We also exclude the Jhelum stream due to evidence of perturbation reported by Bonaca et al. (2019) and Shipp et al. (2019). While we exclude these streams from the LMC mass fitting analysis, we do fit models to Tuc III and Jhelum, including an LMC mass fixed to $1.5 \times 10^{11}\,M_\odot$ in order to examine the possible effect of the LMC on these streams (as in Wan et al. 2020b; Li et al. 2021a).

In order to dynamically model the streams, a clean sample of spectroscopic member stars is needed for the fit. We take the spectroscopic member stars reported in Li et al. (2021a) for ATLAS, Wan et al. (2020b) for Phoenix, and Li et al. (2018) for Tuc III. These three streams all have narrow spatial widths, small velocity dispersions, and unresolved metallicity dispersions; their progenitors are likely to be globular clusters or very low-luminosity dwarf galaxies. The stream membership is usually unambiguous, and member stars are selected subjectively based on their radial velocities, proper motions, metallicities, and locations on the color–magnitude diagram in the reference therein.

For the Jhelum, Indus, and Elqui streams that have a large stream width and whose progenitors are likely to be classical dwarf galaxies (Ji et al. 2020), the membership is less obvious since the streams are embedded in foreground contamination. The stream members are therefore determined with a mixture model including several multivariate Gaussian components in proper motion, radio velocity, and metallicity space, detailed in A. B. Pace et al. (2021, in preparation). We selected highly probable members with membership probability $P_{\rm mem} > 0.8$ from the mixture models as the stream members for this work. Finally, we consider the Chenab stream. Chenab was identified as the southern extension of the Orphan stream by Koposov et al. (2019). S^5 mapped the entire Orphan–Chenab stream within the DES footprint in 2018, and partially observed some of the northern extension in 2019 (Li et al. 2019). Through the rest of this work, we abbreviate the name of the Orphan–Chenab stream as OC. We use a data set that combines the S^5 data with data from Large Sky Area Multi-Object Fiber Spectroscopic Telescope (LAMOST ; Zhao et al. 2012) and Apache Point Observatory Galactic Evolution Experiment (APOGEE; Majewski et al. 2017) to cover more than 100° along the OC stream. Rather than fitting individual member stars, we use spline fits to this data set by S. E. Koposov et al. (2021, in preparation), similar to those of Koposov et al. (2019) for the northern component of the stream. Stream member stars are selected from S^5 works that are published or in preparation.[23] We use the RA, Dec, and proper motion measurements from Gaia EDR3 and the radial velocities from S^5 for these individual member stars as input for the modeling. Specifically, the radial velocities are taken from the second internal data release (iDR2.2) which is described in detail in Ji et al. (2021). We note that, as all the streams presented here except for Tucana III were observed in 2018 by S^5, the radial velocities of the these stream members are also available in the first public release (DR1)[24] of S^5, which is based on an earlier internal data release (iDR1.4; Li et al. 2019) with the same spectral data.

2.3. Distance Measurements

Distance is an important component of 6D phase-space measurements. Although Shipp et al. (2018) measured the distance for all these streams with isochrone fitting, the distance gradients along the streams are much harder to constrain. In this work, we include the distance measurements from individual blue horizontal branch (BHB) stars and RR Lyrae (RRL) stars following the same methods described in Li et al. (2021a). In short, we cross match the spectroscopic stream members with the Gaia RRL catalogs (Holl et al. 2018; Clementini et al. 2019) to find the RRL members in these streams. We then determine the distance modulus of RRL stars using the relation from Muraveva et al. (2018) and dereddened Gaia G-band magnitude. The relation is metallicity dependent; we therefore adopt the mean metallicity of each stream from the literature for the distance determination. We classify stream members with $g - r < 0.1$ and not in RRL catalogs as BHB members. The distance modulus of each BHB star is then calculated using the relation from Belokurov & Koposov (2016) and dereddened DES photometry. In our current sample, we do not see a systematic offset in distance between the two populations of tracers. We assume an uncertainty in distance modulus of 0.17 mag from Muraveva et al. (2018) for RRL stars, and an uncertainty of 0.1 mag from Deason et al. 2011 for BHB stars. We note that we only selected BHB and RRL members from the spectroscopic sample. Although more BHB and RRL members are likely present outside of AAT fields, especially for the dwarf galaxy streams with large stream widths, we limit our selection to the stars that have radial velocities available for a purer sample. We list the number of spectroscopic members along with the number of BHB and RRL members used in each stream in Section 4.3 when we discuss individual streams.

3. Method

3.1. Stream Models

Following the method of Erkal et al. (2019), we model stream formation and evolution using the modified Lagrange Cloud Stripping technique developed in Gibbons et al. (2014). The method consists of releasing test particles at the Lagrange points of the progenitor, and then evolving them in the combined potential of the the progenitor, the Milky Way, and the LMC. As in Erkal et al. (2019), we model both the Milky Way and LMC as individual systems sourcing their respective gravitational potentials, which is crucial for capturing the response of the Milky Way to the LMC.

We represent the Milky Way potential using the results of McMillan (2017), and evaluate the acceleration from the potential using `galpot` (Dehnen & Binney 1998). The McMillan (2017) potential includes six axisymmetric components, namely, bulge, dark matter halo, thin and thick stellar disk, and H I and molecular gas disks. We take the Sun's position, $R_0 = 8.23\,\mathrm{kpc}$, and 3D velocity, $(U_\odot, V_\odot, W_\odot) = (8.4245.7, 7.3)\,\mathrm{km\,s^{-1}}$, from McMillan (2017). As described in Li et al. (2021a) and Wan et al. (2020b),

[23] Note that since the S^5 catalog is continuously updated with new observations and with improvements to the reduction pipeline, the adopted members may change before publication of the final member list in the associated work. However, we do not expect these small differences to change our results.

[24] https://zenodo.org/record/4695135#.YNv_PjZKjdc

Table 1
Priors on MCMC Fit Parameters

Parameter	Prior	Range	Units	Description
$\phi_{2,\mathrm{prog}}$	Uniform	(–1, 1)	deg	Vertical spatial placement of the progenitor in stream coordinates.
σ_{ϕ_2}, prog	Uniform	(0, 2)	deg	Nuisance parameter representing stream spatial width.
$v_{r,\mathrm{prog}}$	Uniform	(–300, 300)	km s^{-1}	Radio velocity of the progenitor.
$\sigma_{v_r,\mathrm{prog}}$	Uniform	(0, 20)	km s^{-1}	Nuisance parameter representing stream velocity dispersion.
$(m-M)_{\mathrm{prog}}$	Normal	$(m-M)_0 \pm 0.2$	mag	Distance modulus of the progenitor.
$\mu_{\phi_1}\star$, prog	Uniform	(–10, 10)	mas yr^{-1}	Proper motion of the progenitor along the stream.
μ_{ϕ_2}, prog	Uniform	(–10, 10)	mas yr^{-1}	Proper motion of the progenitor perpendicular to the stream.
M_{LMC}	Log-uniform	(2, 30)	$10^{10}\,M_\odot$	Total mass of the LMC.
$\mu_\alpha\star$, LMC	Normal	1.91 ± 0.02	mas yr^{-1}	Proper motion of the LMC in RA (Kallivayalil et al. 2013).
μ_δ, LMC	Normal	0.229 ± 0.047	mas yr^{-1}	Proper motion of the LMC in Dec (Kallivayalil et al. 2013).
$v_{r,\mathrm{LMC}}$	Normal	262.2 ± 3.4	km s^{-1}	Radio velocity of the LMC (van der Marel et al. 2002).
d_{LMC}	Normal	49.97 ± 1.13	kpc	Distance of the LMC (Pietrzyński et al. 2013).
M_{prog}	Fixed	⋯	$M_\odot$	Mass of the progenitor (see Table A1).
$r_{s,\mathrm{prog}}$	Fixed	⋯	kpc	Scale radius of the progenitor (see Table A1).

in order to examine the effects of the choice of Milky Way potential model on our stream fits, we produce ten realizations of this potential by sampling the Markov Chain Monte Carlo (MCMC) chains from the fit in McMillan (2017). We find that the least massive of these realizations ($M_{\mathrm{MW}} = 8.3 \times 10^{11}\,M_\odot$) provides the best fit to the stream data. We provide the potential parameters in Table A3 in the same format as McMillan (2017).

We model the mass distribution of the LMC as a stellar disk and a dark matter halo. The stellar disk is modeled as a Miyamoto–Nagai disk (Miyamoto & Nagai 1975) with a mass of $3 \times 10^9\,M_\odot$, a scale radius of 1.5 kpc, and a scale height of 0.3 kpc. The orientation of the LMC disk matches the measurement of van der Marel & Kallivayalil (2014). The LMC's dark matter halo is modeled as a Hernquist profile (Hernquist 1990). As in Erkal et al. (2019), we leave the total mass of the LMC as a free parameter but fix the scale radius to match the circular velocity measurement of 91.7 km s^{-1} at 8.7 kpc from van der Marel & Kallivayalil 2014. Note that this is in agreement with more recent measurements of the LMC's circular velocity (e.g., Cullinane et al. 2020). The total mass and shape of the LMC potential is fixed throughout each simulation, and does not evolve after infall. We account for the dynamical friction of the Milky Way on the LMC using the results of Jethwa et al. (2016). We also fit for the proper motion, distance, and radio velocity of the LMC with priors given by their observed value and uncertainty (Table 1; van der Marel et al. 2002; Kallivayalil et al. 2013; Pietrzyński et al. 2013).

We model the potential of each stream's progenitor as a Plummer sphere (Plummer 1911) with a mass and scale radius chosen to match the observed stream width. During the course of tidal disruption, the progenitor's mass decreases linearly in time to account for tidal stripping. The majority of the streams considered in this work do not have a known progenitor, so we assume that the progenitor has completely disrupted, i.e., that its present day mass is zero. Furthermore, for the majority of streams, we assume that the remnant of the progenitor is in the middle of each stream's observed extent. The only exceptions are Tuc III and OC. Tuc III is one of the few streams known to be associated with a bound progenitor. For this stream, we require a bound progenitor to remain at present day, positioned at $(\phi_1, \phi_2) = (0^\circ, 0^\circ)$ in the stream coordinates of Tuc III. For OC, the progenitor is placed at $\phi_1 = 6.^\circ34$ in the coordinate system from Erkal et al. (2019) and Koposov et al. (2019). This is near the center of the full OC stream, and is the same progenitor position as in Erkal et al. (2019). For all streams we use coordinate systems defined by the rotation matrices in Appendix D of Shipp et al. (2019), with the exception of OC, for which we use the coordinate system defined by Koposov et al. (2019).

3.2. Comparison with Data

We calculate the likelihood of each stream model by producing mock observations of the simulated stream and comparing them with the data set described above. For each stream model, we calculate the track on the sky, the radial velocity, the proper motions in RA and Dec, and the distance as functions of ϕ_1, the observed angle along the stream. The likelihood is calculated for each S^5 member star, as described in Section 3.2 of Erkal et al. (2019), using simulated particles within $\pm 1^\circ$ in ϕ_1 of each S^5 member. When calculating the likelihood of the stream track and radio velocity of each star, we take into account not only the measurement uncertainty of each star, but also the intrinsic width and stellar velocity dispersion. We introduce two nuisance parameters (σ_{ϕ_2}, σ_{vr}), which are added in quadrature to the intrinsic width and velocity dispersions of the model. These parameters can account for possible perturbations that are not included in the model, and also allow for slight variations in the stream model to better fit the observed data without varying the progenitor mass. We assign the total mass of each progenitor in order to roughly reproduce the observed width of each stream by eye. The progenitor parameters are listed in Table A1.

We perform a MCMC fit using `emcee` (Foreman-Mackey et al. 2013). Our model includes 12 free parameters, namely, the ϕ_2 position, distance, radio velocity, and proper motion of the progenitor at present day, the stream track and radio velocity nuisance parameters, and the proper motion, radial velocity, distance, and total mass of the LMC. The prior distributions on each parameter are listed in Table 1. The upper limit of our prior on the LMC mass is selected to ensure that the LMC is on its first infall within our Milky Way potential, based on tests we performed of various LMC masses in our Milky

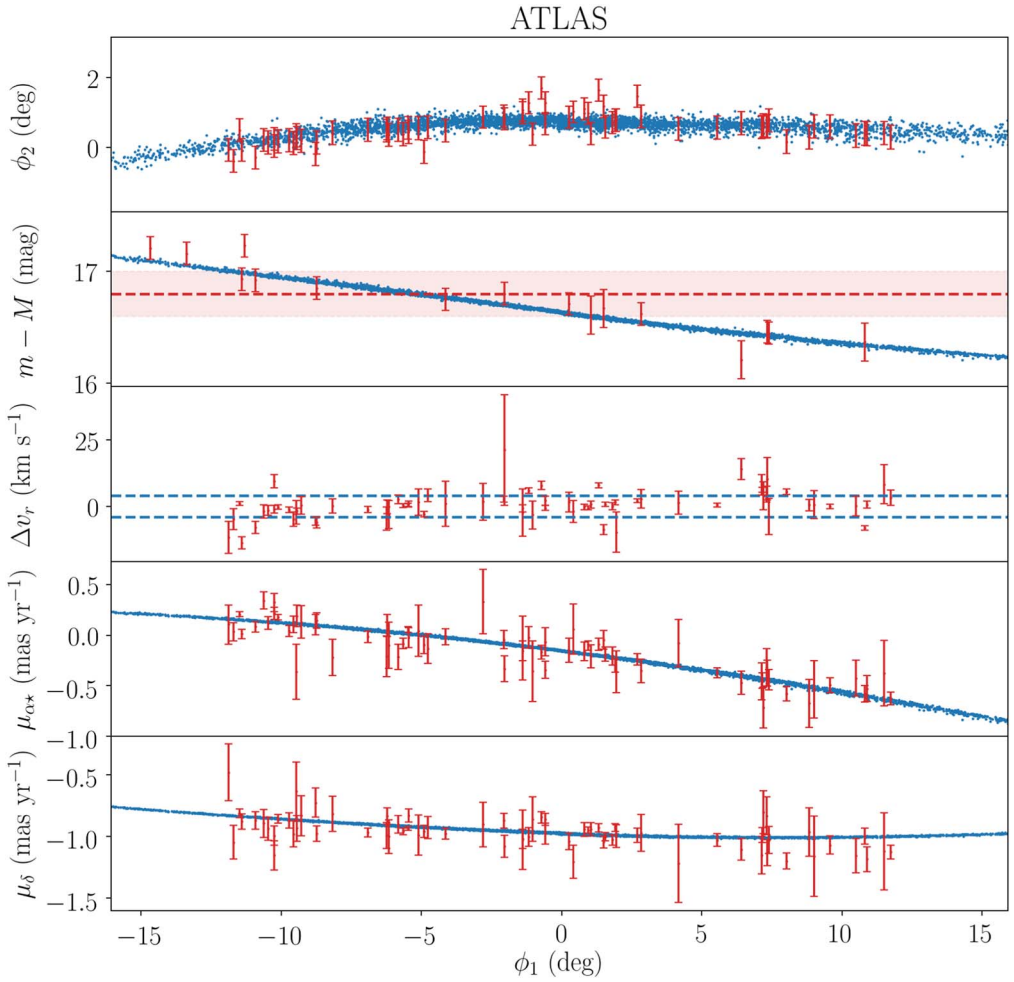

Figure 1. Model fit to the ATLAS stream. The simulated stream is shown in blue, and the S^5 members included in the MCMC fit are plotted in red. In the first panel, we present the track in stream coordinates (ϕ_1, ϕ_2), calculated using the rotation matrices from Shipp et al. (2019) and the RA and Dec measurements from Gaia EDR3. The error bars on the data represent the total stream width fit to the data. In the second panel, we show the distance modulus along the stream. The dashed red line and shaded region represent the distance measurement from Shipp et al. (2018) with a 0.2 mag uncertainty, and the individual points represent the BHB star and RRL star distance tracers included in the fit. In the third panel, we plot the difference between the measured and model radial velocity at the ϕ_1 position of each member star. The separation of the blue dashed lines is equal to two times the total velocity dispersion fit to the data. The fourth and fifth panels show the proper motions of the model and the measured proper motions of the S^5 member stars from the Gaia EDR3 data set. Similar figures for each stream are included in Appendix B.

Way potential. The priors on the stream progenitor properties are selected to be uninformative.

4. Results

Following the method described above, we fit models to each stream and obtain five independent constraints on the total mass of the LMC. As a demonstration of the stream models in comparison to the data, we show the best-fit model to the ATLAS stream in Figure 1. The red points are the S^5 members and the blue points represent the stream model. This shows that the best-fit model can recover all of the observed trends in the ATLAS stream. Similar figures for the other streams are included in Appendix B. The data for each stream model can be found at this link.[25] In addition, a movie showing the orbits of the seven streams included in this work and the LMC can be found at this link.[26]

In this section, we present the measurements of the mass of the LMC, and discuss the details of the interaction between each stream and the LMC in order to develop a consistent picture of how the Milky Way's largest satellite has perturbed this population of stellar streams.

The constraints on the LMC mass are presented in Table 2 and Figure 2. Constraints on the other progenitor and LMC parameters are included in Table A1. In Figure 2, each color represents the posterior distribution on the LMC mass resulting from the fit to each stream and marginalized over the other fit parameters. The dark blue shaded region represents the best-fit LMC mass and uncertainty from an analysis of the OC stream (Erkal et al. 2019), and the light blue shaded region represents LMC mass inferred from fits to the Sagittarius stream (Vasiliev et al. 2021). Generally, the results are consistent with each other and the two previous measurements to within 1σ. We thus combine the individual measurements to provide a joint constraint on the LMC mass, which is displayed as the gray shaded region and described in Section 4.4. We note that the posterior distribution for the Phoenix stream is very broad and provides no meaningful constraint on the LMC mass.

[25] https://zenodo.org/record/5507238#.YUCpO55KhTY
[26] https://www.youtube.com/watch?v=CrYhjJ-u5RA

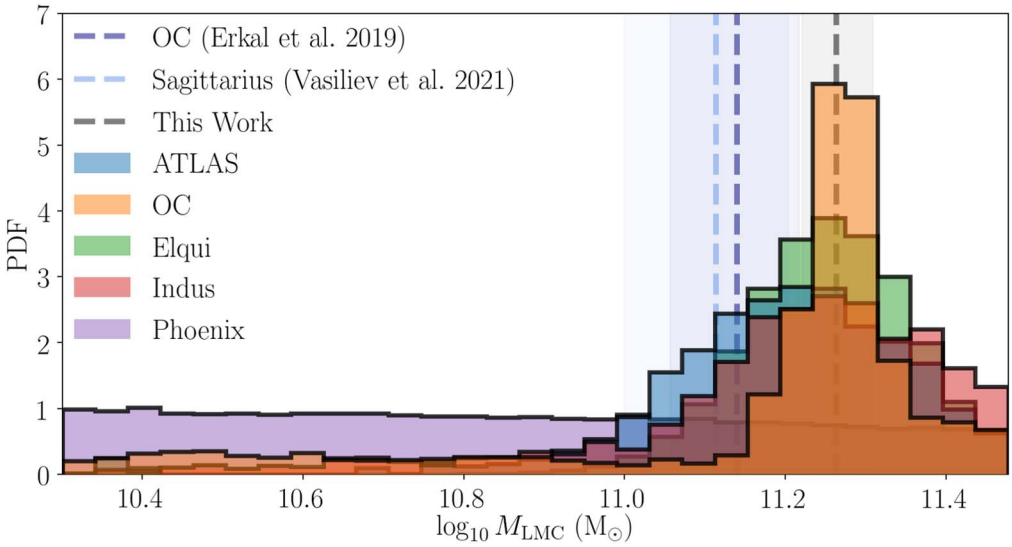

Figure 2. Marginalized posterior distributions on the total LMC mass from fits to each of the five streams. The dark blue vertical dashed line and shaded region show the constraint on the LMC mass from the fit to the OC stream in Erkal et al. (2019), the light blue dashed line and shaded region represent the measurement using the Sagittarius stream by Vasiliev et al. (2021), and the gray dashed line and shaded region represent the combined mass constraint from the five measurements presented in this work.

Table 2
LMC Mass Measurements and Parameters of the Closest Approach

Stream	$M_{\rm LMC}$ (10^{10} $M_\odot$)	$r_{\rm approach}$ (kpc)	$v_{\rm approach}$ (km s^{-1})	$t_{\rm approach}$ (Myr)
ATLAS	$14.3^{+6.7}_{-3.5}$	23.9	467.1	80.0
OC	$18.8^{+3.5}_{-4.0}$	25.4	371.2	310.0
Elqui	$16.8^{+5.2}_{-3.0}$	11.2	419.6	99.0
Indus	$15.6^{+8.6}_{-3.6}$	38.0	268.5	10.5
Phoenix	$2.7^{+8.5}_{-0.7}$	30.7	433.9	49.2
Tucana III	···	4.2	382.4	98.8
Jhelum	···	40.6	367.2	2.8

4.1. Physical Intuition

Stream perturbations can manifest as a difference between the spatial and velocity components. This can be observed as a misalignment between the proper motion ($\mu_{\phi_2}/\mu_{\phi_1}$) and stream track ($d\phi_2/d\phi_1$), or as an offset between the radial velocity (v_r/μ_{ϕ_1}) and distance ($dD/d\phi_1$) gradients along the stream (see Section 4.2 for more details). The current data are most sensitive to the on-sky perturbation (i.e., offsets between the proper motion and stream track) because distance gradients measured along the stream are relatively imprecise. Thus, our constraints on the LMC mass depend both on the strength and direction of the LMC perturbation.

Given the orbits of each stream, we can predict the magnitude of the perturbation on the system by the LMC. Streams that pass close to the LMC with a small relative velocity are predicted to experience the strongest perturbations. For each stream, Table 2 lists the distance of closest approach to the LMC, the relative velocity between the stream and the LMC at closest approach, and the time at which this interaction occurs. The 95% confidence interval on each LMC mass measurement is calculated from the highest density interval of the posterior distribution. With these parameters, we can predict the magnitude of the perturbation, as illustrated in Figure 3.

Figure 3 shows the distance of closest approach and the relative velocity for several points along each stream, spaced by 0.1° in ϕ_1. The curves represent lines of constant perturbation strength, assuming the interaction is impulsive, using the results of Section 3.1 of Erkal & Belokurov (2015),

$$\Delta v = \frac{GM}{bw}, \tag{1}$$

where b is the impact parameter, w is the relative velocity, and Δv is the velocity kick to the stream. Streams that pass very close to the LMC with a small relative velocity are predicted to experience the largest perturbation, therefore Tuc III, Elqui, and OC should experience a more significant perturbation by the LMC than ATLAS, Phoenix, Indus, and Jhelum.

As described above, the interaction geometry is also an important consideration in predicting the effect of the LMC on each stream, since different perturbation geometries will affect different observables. Given the precise measurements of the proper motions, radial velocities, and in particular, the stream tracks from Gaia and S^5, and the relative imprecision of the distance measurements, we will most easily be able to identify perturbations manifesting as changes to the stream proper motion and track.

We can characterize the observable effect of the LMC on a given stream by approximating the perturbation as a velocity kick toward the LMC at the point of closest approach. We then break down this velocity kick into components along the direction of the angular momentum, radial, and tangential vectors of the stream's orbit with respect to the Milky Way. This geometry is illustrated in Figure 4. Velocity kicks out of the orbital plane, along the direction of the angular momentum vector of the stream's orbit, will produce an offset between the track of the stream and the direction of the proper motion, which can be precisely measured with the S^5 and Gaia data. Kicks in the radial direction will manifest as an offset between the radial velocity and the distance gradient, which is more difficult to measure due to the difficulty in measuring distances

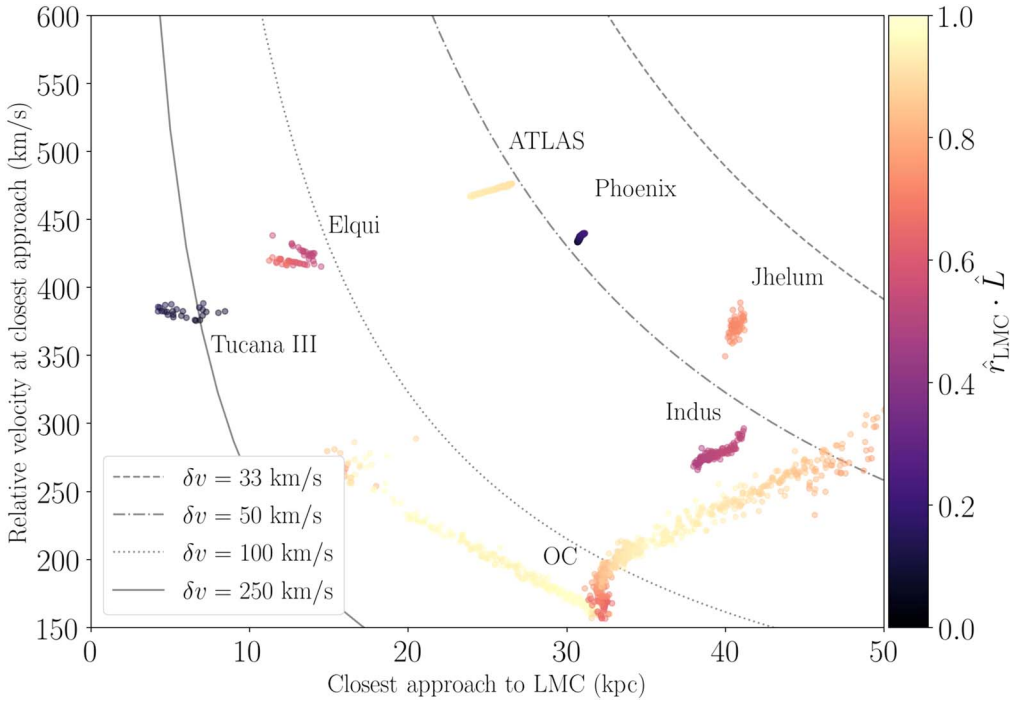

Figure 3. Predicted perturbation by the LMC on each stream. The x-axis shows the distance of closest approach, and the y-axis is the relative velocity at closest approach. For each stream, we plot points spaced by $0.^{\circ}1$ in ϕ_1. The curves represent lines of constant perturbation, assuming the interaction is impulsive. The color represents the component of the velocity kick in the direction of the angular momentum vector. Kicks in this direction present as offsets between the stream track and the proper motion direction, which are most easily measurable given currently available data.

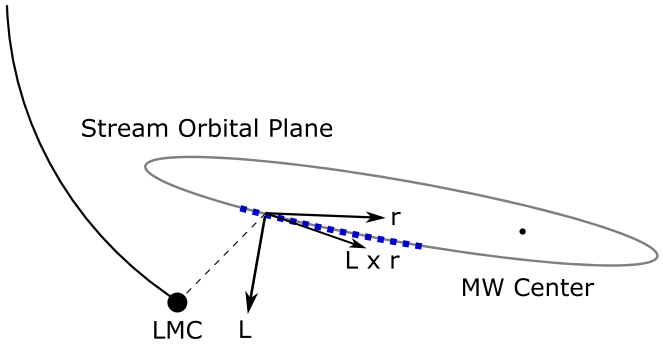

Figure 4. The interaction geometry between a stream and the LMC. The blue dotted line represents a stream within an orbital plane traced by the solid black oval. The black dashed line represents the vector between the stream and the LMC at closest approach. We decompose this vector into components aligned with the angular momentum vector of the stream's orbit ($\hat{L}$), the radial vector between the stream and the Galactic center ($\hat{r}$), and a third perpendicular vector tangential to the stream's orbit ($\hat{L} \times \hat{r}$).

along each stream. Perturbations aligned with the stream's velocity will be the most difficult to measure.

The color scale in Figure 3 represents the projection of the predicted perturbation in the angular momentum direction. Since perturbations in this direction are the most easily observable, this is a proxy for how observable the LMC's effect will be for the streams in our data set. Figure 5 gives a more detailed view of the three components of the predicted perturbations. Streams with the largest kicks in the angular momentum direction (yellow) are predicted to provide the strongest constraints on the LMC mass, while streams with small perturbations overall, or where the perturbations are primarily in the radial or tangential directions will provide weaker constraints. Interestingly, OC and ATLAS have the largest predicted perturbations out of the orbital plane, which coincides with the significant proper motion offsets measured for these streams (e.g., Erkal et al. 2019; Koposov et al. 2019; Shipp et al. 2019; Li et al. 2021a).

4.2. Offsets

In order to examine the predicted and measured effect of the LMC on each stream we compare the orientation of the stream to the direction of motion (e.g., Erkal et al. 2019; de Boer et al. 2020; Li et al. 2021a). Unperturbed streams roughly follow simple orbits and move in the direction in which they are extended. By combining Gaia and S^5 data, we can compare the direction of motion to the extension of each stream in two ways. First, we can compare the track of the stream on the sky to the direction of its proper motion. Second, we can compare the distance gradient along the stream (along ϕ_1) to the ratio of the radial velocity and the proper motion in the ϕ_1 direction. These comparisons are illustrated in Figures 6 and 7. The lines in these figures are each fit using cubic splines, following the MCMC method described in Section 3.1 of Erkal et al. (2017). The shaded bands represent the 1σ uncertainties resulting from the MCMC spline fit.

Figure 6 shows the offsets between the stream tracks and the direction of the proper motion for each stream in the model (blue) and the data (red). In each figure the dashed lines show the slope of the stream track $\left(\frac{d\phi_2}{d\phi_1}\right)$, and the solid lines represent the ratio of the reflex-corrected proper motions ($\mu_{\phi_2}/\mu_{\phi_1}$) along the stream. We note that in this ratio we have used the quantity $\mu_{\phi_1} = \frac{d\phi_1}{dt}$, which does not have a $\cos\phi_2$ term. Due to the reflex correction applied to the proper motions, the uncertainties on the ratios incorporate both proper motion and distance uncertainties, which we find to be of comparable magnitude.

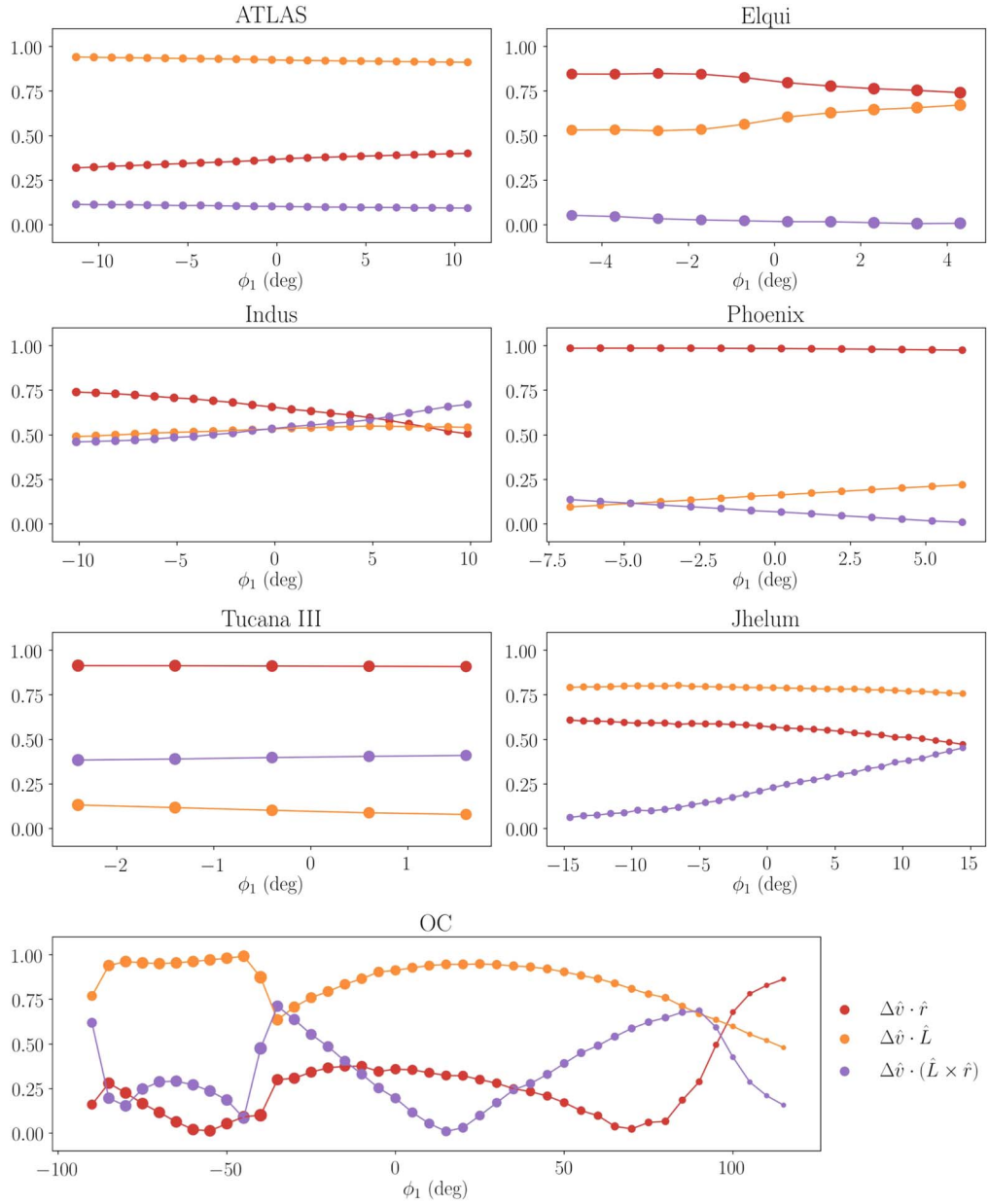

Figure 5. Velocity kicks normalized to unity in three directions for each stream, assuming an impulsive interaction. Yellow represents the direction of the angular momentum of the stream orbit, red represents the radial direction (toward the center of the Milky Way) and purple represents the direction tangential to the stream orbit. Offsets in the angular momentum direction are the most visible given currently available data. Therefore, streams with large offsets in that direction, such as OC, are predicted to provide the strongest constraint on the LMC mass.

Unperturbed streams should have no offset between the solid and dashed lines, while streams perturbed out of their orbital plane are predicted to have a significant offset. The offsets in the models roughly match the scale of the corresponding offsets in the data. Differences in the shapes of the curves may be due to lack of complexity in the model (e.g., additional small-scale perturbations), or the effect of placing the progenitor at $\phi_1 = 0°$. In the data (red), OC, ATLAS, and Elqui have the largest offsets between the two lines (note the differing axis scales between panels), which is consistent with the predictions illustrated in Figure 5.

Figure 7 shows the offsets in the radial direction. Here, the dashed line represents the distance gradient along the stream $\left(\frac{dr}{d\phi_1}\right)$, while the solid line represents the ratio of the reflex-corrected radial velocity to the reflex-corrected proper motion along the stream (v_r/μ_{ϕ_1}). Once again, unperturbed streams should show no offsets between these two lines, while streams perturbed in the radial direction should show significant offsets. The stream with the largest predicted offset in the model is Tuc III. This suggests that with improved distance measurements, and accounting for the possible effect of the Milky Way bar, we may be able to use Tuc III to place strong constraints on the mass of the LMC.

4.3. Individual Streams

4.3.1. ATLAS

The ATLAS stream is a narrow stellar stream that was first discovered in the VST ATLAS survey (Koposov et al. 2014),

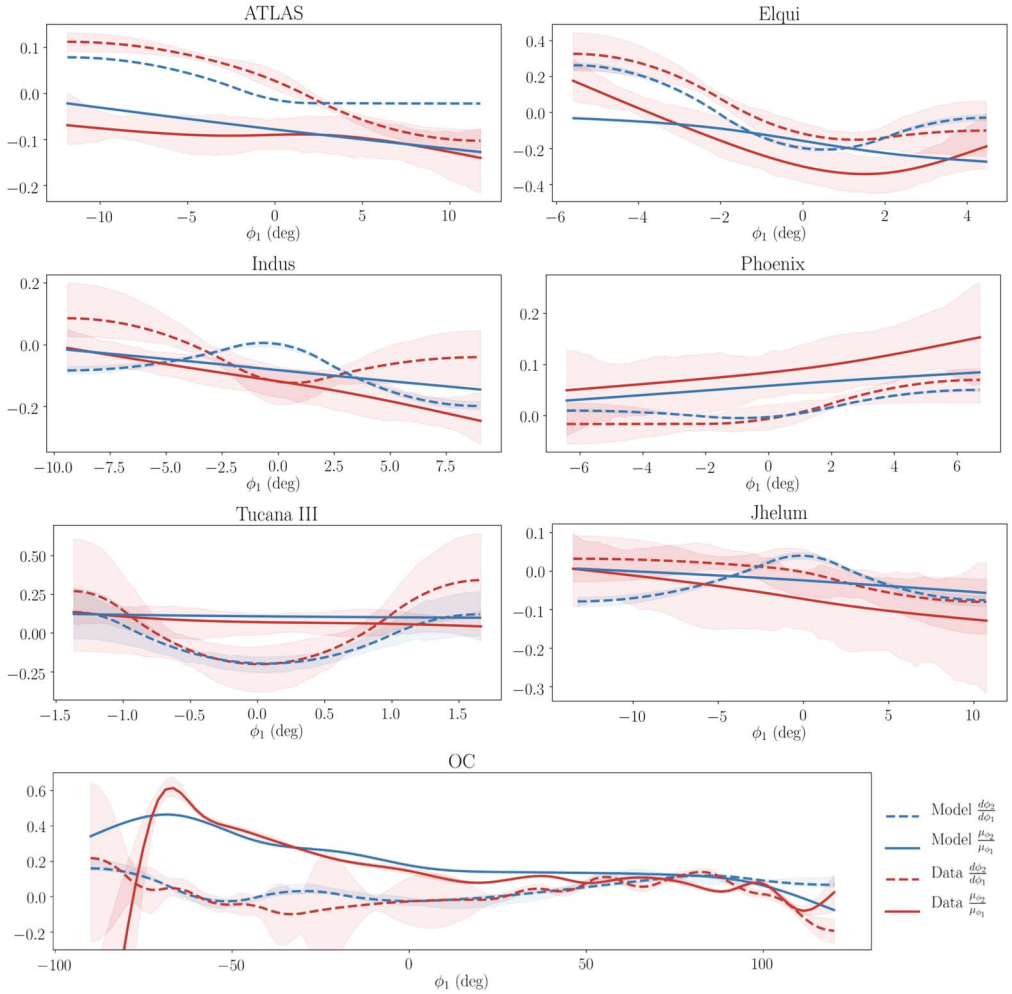

Figure 6. Offsets between the proper motion and the track of each stream. Solid lines represent the ratio of the proper motions ($\mu_{\phi_2}/\mu_{\phi_1}$), and the dashed lines represent the slope of the track on the sky. Blue lines/shaded regions correspond to the best-fit model, and red lines/shaded regions correspond to the S^5 data. The shaded regions represent the 1σ uncertainties on each curve. For an unperturbed stream on a simple orbit, the dashed and solid lines will be aligned. However, several of these streams show some offset. OC, as predicted, has the largest proper motion offset, in both the data and the model.

and further studied with deeper data from DES (Shipp et al. 2018), and with spectroscopic data from S^5 (Li et al. 2021a).

Our model of the ATLAS stream is fit to the 72 S^5 members identified by Li et al. (2021a). In addition, we include distance measurements to 13 BHB stars and five RRL stars in the calculation of the likelihood. The best-fit model for ATLAS is shown in Figure 1. As noted in Section 3, we exclude Aliqa Uma, which has been shown to be an extension of the ATLAS stream (Li et al. 2021a), separated by a small perturber that has passed close to the stream.

Our fit to the ATLAS stream provides a measurement of $M_{\rm LMC} = 14.3^{+6.7}_{-3.5} \times 10^{10}\,M_\odot$. Li et al. (2021a) also fit a model to the ATLAS stream, including an LMC with a fixed mass of $15 \times 10^{10}\,M_\odot$. This is within 1σ of our LMC mass measurement, and it is therefore unsurprising that Li et al. (2021a) obtained a good fit to the ATLAS stream including this fixed LMC mass and that their derived orbital properties are consistent with our best-fit orbit.

Figure 3 and Figure 5 show that ATLAS has one of the smaller predicted total perturbations, but one of the larger perturbations out of its orbital plane, suggesting that the majority of the perturbation should be observable as an offset between the track and proper motion of ATLAS. This is consistent with the large observed proper motion offset in ATLAS (Shipp et al. 2019; Li et al. 2021a), and explains why ATLAS provides one of the strongest constraints on the LMC mass.

4.3.2. OC

The northern part of the OC stream was discovered in SDSS by Grillmair (2006) and Belokurov et al. (2006). Chenab, the southern portion of OC, was then discovered in DES by Shipp et al. (2018) and was later determined to be an extension of the Orphan stream by Koposov et al. (2019). Here, we fit the full observed stream, using splines fit to data from S^5, LAMOST, and APOGEE (S. E. Koposov et al. 2021, in preparation).

The southern component of OC has one of the largest predicted total perturbations by the LMC, and the largest along its angular momentum vector. Therefore, OC is expected to provide the strongest constraint on the LMC mass of the five streams included in this work. As seen in Figure 2, OC does in fact provide one of the tightest constraints.

Figure 3 illustrates how the impact of the LMC on OC varies along the length of the stream. The strongest predicted impact is along the southern portion of the stream. This part of the stream is also most significantly perturbed out of its orbital

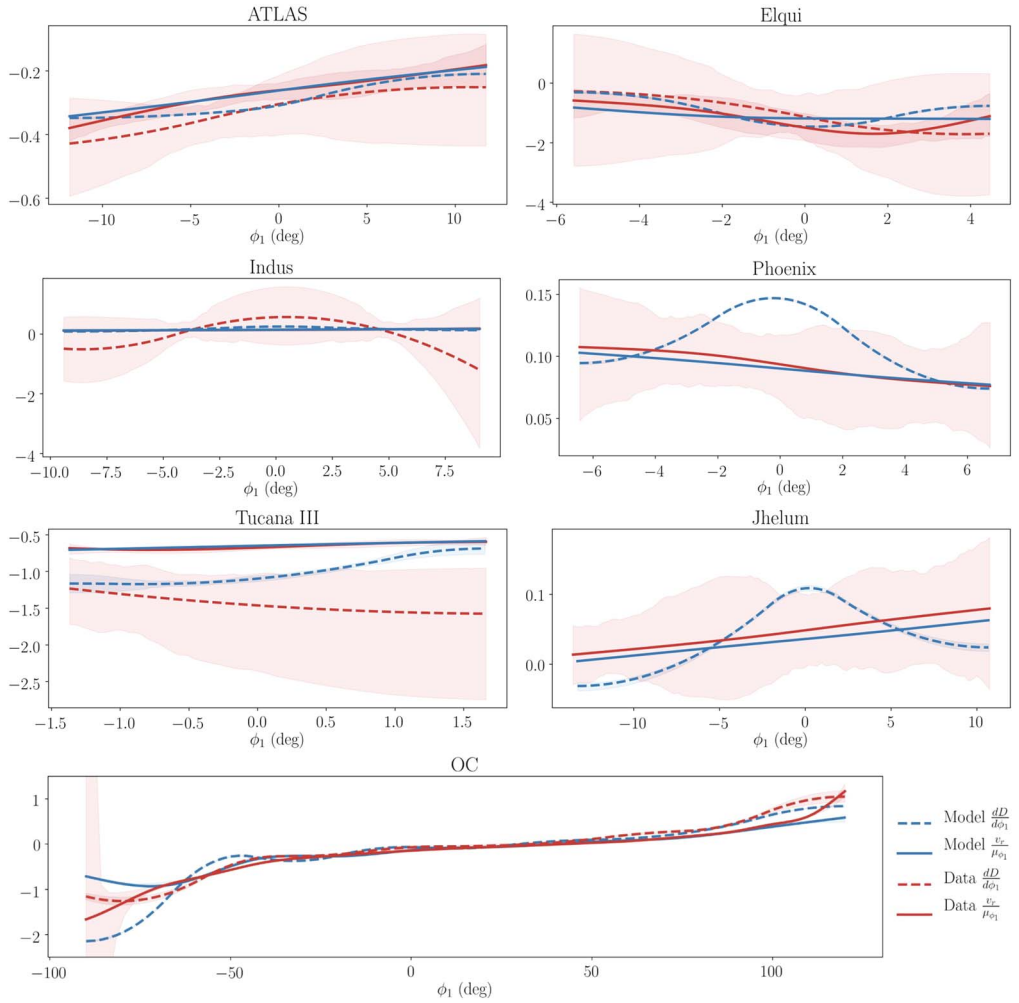

Figure 7. Offsets between the radial velocity and distance gradient of each stream. Solid lines represent the ratio of the solar reflex-corrected radial velocity to the proper motion (v_r/μ_{ϕ_1}) along each stream, and the dashed lines represent the distance gradient. As in the above figure, blue lines correspond to the model, and red lines correspond to the data. We exclude the distance gradients for the Phoenix and Jhelum data due to large uncertainties. None of the streams have sufficient data to measure a significant offset between the two red lines. Tuc III is the only stream with a large predicted offset in the model. We find that the magnitude of this offset increases with larger LMC masses.

plane (Figure 5), which is consistent with the large proper motion offset seen in Figure 6. Fardal et al. (2019) identify a misalignment between the spatial track and velocity vector along the northernmost component of the stream, which is consistent with the offset shown at large ϕ_1 in Figure 7. At $\phi_1 > 125°$, we see an offset in both the data and the model between the distance gradient and the ratio of the radial velocity to the proper motion along the stream, which suggests the stream is curving away in distance at a greater rate than would be expected along an unperturbed orbit.

We obtain a best-fit value of $M_{\rm LMC} = 18.8^{+3.5}_{-4.0} \times 10^{10}\,M_\odot$, which differs from the result of Erkal et al. (2019) by $\sim 1\sigma$. This offset may be due to differences in data set or model. We discuss the possible sources of this difference in greater detail in Section 5.

In fitting the OC stream, we find the resulting LMC mass depends somewhat on the placement of the progenitor along the stream. Placing the progenitor along the portion of the stream discovered in the DES footprint resulted in a larger LMC mass. However, the total enclosed LMC mass within the closest passage of the progenitor in each case changes only slightly. This is due in part to the fact that we fix the scale radius of the LMC in order to match the circular velocity measurement from van der Marel & Kallivayalil (2014). The influence of the progenitor placement may therefore be mitigated by introducing more flexibility in the outskirts of the LMC potential.

4.3.3. Elqui

Elqui was discovered by Shipp et al. (2018) in the DES data, and is the most distant of the DES stellar streams at 50 kpc. Our list of likely Elqui members includes 43 S^5 stars, with three BHB stars and five RRL stars, which we fit to constrain the mass of the LMC to $M_{\rm LMC} = 16.8^{+5.2}_{-3.0} \times 10^{10}\,M_\odot$. Elqui passes within 15 kpc of the LMC and shows signs of significant perturbation. In particular, the track of Elqui appears to deviate from the great circle orbit that passes through the two endpoints, as viewed from the Sun (Figure B1). This deviation can be reproduced by a model including a massive LMC, but cannot be reproduced if the LMC is excluded. Elqui has a significant predicted perturbation in the angular momentum direction, but the largest predicted velocity kick is in the radial direction. This suggests that with improved distance

measurements we may be able to use Elqui to place an even stronger constraint on the LMC mass.

Elqui is measured to have a large velocity dispersion of $16.8\,\mathrm{km\,s^{-1}}$ (Li et al. 2021b). For comparison, streams with similar predicted progenitor masses, such as Indus, have typical velocity dispersions of $<10\ \mathrm{km\,s^{-1}}$. This large dispersion is also present in the best-fit stream model. This is despite the fact that our progenitor for Elqui is dynamically cold, with a mass of only $M_{\mathrm{prog}} = 10^6\,M_\odot$. This indicates that the measured stream dispersion does not necessarily map directly onto the dispersion of the progenitor system. It seems unlikely that this unusually large dispersion is due to perturbation by the LMC, as it does not significantly decrease with decreasing LMC mass. The large dispersion may be due to the high orbital eccentricity of Elqui. The source of this large dispersion requires further investigation.

Shipp et al. (2018) proposed a possible connection between Elqui and the Magellanic Clouds, due to the similar distance and orientation of Elqui to the Magellanic Clouds and Stream, respectively. Shipp et al. (2019) showed that the proper motion of Elqui is inconsistent with an association with the Magellanic stream. We further support this conclusion here, noting that at closest approach, Elqui has a velocity relative to the LMC of $\sim 420\ \mathrm{km\,s^{-1}}$, indicating that it cannot be bound to the Magellanic system.

4.3.4. Indus

The Indus stream is a thick stream discovered by Shipp et al. (2018) in DES. Our list of likely Indus members consists of 59 S^5 stars, including four BHB stars and one RRL star, which we fit to measure an LMC mass of $M_{\mathrm{LMC}} = 15.6^{+8.6}_{-3.6} \times 10^{10}\,M_\odot$. Of the five streams used to fit the LMC mass, Indus has the largest distance of closest approach to the LMC. However, it passes by at a slow relative velocity and with a geometry such that the predicted velocity kick in the angular momentum direction is similar in magnitude to that of ATLAS or Elqui. Indus is predicted to have experienced a radial perturbation equal in magnitude to its perturbation out of its orbital plane. Indus also has only a small number of known distance tracers, and therefore a large uncertainty in its distance gradient. Given the large width of Indus, it is likely that additional distance tracers lie outside the limits of the S^5 footprint. With an improved measurement of the distance gradient, it is likely that Indus can provide an even stronger constraint on the LMC mass.

4.3.5. Phoenix

Phoenix is a narrow stream discovered in the DES data by Balbinot et al. (2016) and further studied by Shipp et al. (2018). Significant density variations of unknown origin have been identified along the stream (Balbinot et al. 2016; Tavangar et al. 2021). These variations are unlikely to be due to a large-scale perturbation by a system like the LMC. Wan et al. (2020b) found that Phoenix has a very low metallicity ([Fe/H] ≈ -2.7 dex), suggesting that Phoenix represents the tidal debris of the most metal-poor Milky Way globular cluster known to date.

Phoenix has the least sensitivity to the LMC mass of the five streams, as seen in Figure 2. We fit the 30 S^5 members of Phoenix, as published in Wan et al. (2020b), and three BHB stars to obtain an LMC mass measurement of $M_{\mathrm{LMC}} = 2.7^{+8.5}_{-0.7} \times 10^{10}\,M_\odot$. It is unsurprising that Phoenix provides a weaker constraint on the LMC mass than the other streams, for two primary reasons. First, the Phoenix stream has the smallest predicted velocity kick from the LMC, as shown in Figure 3. Only Indus has a larger distance of closest approach to the LMC, and Phoenix passes by the LMC with a much larger relative velocity. Second, the orientation of the Phoenix stream relative to the LMC suggests that the majority of the velocity kick is in the radial direction, as seen in Figure 5, and is thus very difficult to detect with current observations. This suggests that with an improved distance gradient we may be better able to measure the effect of the LMC on the Phoenix stream, and perhaps tighten the constraint on the mass of the LMC.

4.3.6. Tucana III

Tuc III was discovered in the second year of DES data by Drlica-Wagner et al. (2015) and consists of thin tidal tails extending from a central progenitor. We exclude Tuc III from this analysis due to its probable interaction with the Milky Way bar, as discussed in Section 2.2. However, Tuc III is an interesting stream to consider in the context of the LMC since it passes within 10 kpc of the LMC. We fit a model to Tuc III including an LMC with a mass fixed to $15 \times 10^{10}\,M_\odot$, motivated by the results of Erkal et al. (2019).

Erkal et al. (2018) modeled the Tuc III stream and predicted the proper motion offset that would be revealed with the release of Gaia DR2. They predicted a large value of the reflex-corrected proper motion perpendicular to the stream, μ_{ϕ_2}, would be observed for any LMC mass greater than $\sim 10^{10}\,M_\odot$. However, the observed proper motion is found to be generally aligned with the track of the stream (Shipp et al. 2019). This inconsistency may be a result of how the Milky Way potential was modeled by Erkal et al. (2018). The LMC is known to induce a significant reflex motion in the Milky Way (e.g., Gómez et al. 2015; Garavito-Camargo et al. 2019; Erkal et al. 2021; Petersen & Peñarrubia 2021); however, Erkal et al. (2018) fixed the centroid of the Milky Way potential, which may have biased the fits to Tuc III and thereby the predictions for μ_{ϕ_2}. In this paper, we allow the center of the Milky Way to move in response to the LMC, and find that we are able to obtain a good fit to the data without a significant proper motion offset. Instead, we find that Tuc III is predicted to have a large offset between its radial velocity and distance gradient (see Figure 7). This predicted offset suggests that a precise measurement of the distance gradient along Tuc III, along with an understanding of the effects of the Milky Way bar, may enable strong constraints on the LMC mass. However, improved distance gradient measurements are difficult due to the distance and low luminosity of the stream. Therefore, despite Tuc III's close passage to the LMC its utility as a probe of the LMC mass is unclear.

4.3.7. Jhelum

Jhelum is a thick stream discovered in the DES data by Shipp et al. (2018). As with Tuc III, we have excluded Jhelum from our analysis due to the evidence of perturbation presented by Bonaca et al. (2019) and Shipp et al. (2019). In particular, Bonaca et al. (2019) identified two distinct spatial components in Jhelum—a thin dense component and a broader, more diffuse component—while Shipp et al. (2019) identified two

distinct proper motion components in Jhelum in the Gaia data. The cause of this unique morphology remains unknown. Despite this evidence of perturbation, we fit a model to Jhelum with a fixed LMC mass of $15 \times 10^{10}\,M_{\odot}$ in order to explore the predicted impact of the LMC. We find that Jhelum is not predicted to be significantly perturbed by the LMC.

4.4. Combined Measurement

This work is the first step toward using a population of streams to measure the potential of the LMC. Ultimately, we would like to combine the measurements of multiple stellar streams in order to increase the precision of our measurement of the LMC potential. However, there are several challenges associated with combining the measurements presented here. First, we chose to fit the streams individually in order to examine the effect of the LMC on each individual system and to develop an understanding of how different streams are perturbed by the LMC depending on their relative orbits and times of closest approach. In addition, combining posterior distributions leads to overcounting of the priors that were repeated in each fit. With these caveats in mind, and primarily for illustrative purposes, we can combine the individual stream measurements by taking the product of Kernel Density Estimates fit to the posterior distributions of the individual streams. From this simple procedure, we derive a combined measurement of the LMC mass of $18.4^{+1.8}_{-1.9} \times 10^{10}\,M_{\odot}$. This measurement differs from the result of Erkal et al. (2019) by 1.3σ and the result of Vasiliev et al. (2021) by 1.5σ. In addition, by combining measurements from multiple streams, we obtain uncertainties on the LMC mass that are smaller than those of either of the previous measurements. In the future, we will simultaneously model a population of streams in order to fit an aspherical, deforming LMC potential, e.g., with basis function expansions (Garavito-Camargo et al. 2021).

5. Discussion

We have fit the mass of the LMC independently using five stellar streams with data from S^5, Gaia EDR3, and DES DR1. In Section 4, we present the constraint on the LMC mass from each of these fits (Figure 2), and discuss the unique interactions between each stream and the LMC (Figures 3 and 5). Here, we place these measurements in context. We discuss how these measurements begin to establish a consistent picture of the influence of the Milky Way's largest satellite on the population of southern stellar streams, draw comparisons to other measurements, and discuss future efforts to model a realistic LMC and Milky Way potential.

As discussed in Section 4, due to the precision of the Gaia EDR3 proper motion measurements, our data are most sensitive to perturbations out of the stream orbital plane, which produce observed misalignments between stream tracks and proper motions. Therefore, by combining the results of Figures 3 and 5, which demonstrate the predicted magnitude and geometry of the perturbation of the LMC on each stream, we can predict the ability of each stream to constrain the mass of the LMC. These predictions suggest that OC, followed by Elqui, ATLAS, and Indus should have the largest observed proper motion offsets and should provide the strongest constraints on the LMC mass. In fact, these are the streams that we find provide the strongest constraints. Streams with large offsets in other directions may require additional data in order to better constrain the LMC mass. For example, Tuc III, Elqui, and Phoenix all have large predicted offsets in the radial direction, which are detectable only with precise measurements of the distance gradient along the stream. The constraints on the LMC mass should show significant improvement with improved distance measurements, which may be obtained in the future with additional distance tracers (as discussed in Section 4.3), deeper photometric data, or the extension of precise parallax measurements to more distant sources. Given these predictions, it is also unsurprising that Phoenix does little to constrain the LMC mass, given it has both the smallest predicted total perturbation, and is predicted to have been perturbed primarily in the radial direction.

By examining the orbits of each stream relative to the LMC, we have assembled a consistent picture of the effect of the LMC on this population of stellar streams. This consistency supports our measurements of a massive LMC with $M_{\rm LMC} \sim 1.8 \times 10^{11}\,M_{\odot}$. We find that all of the streams considered in this work, with the exception of Phoenix, prefer a total mass of the LMC consistent with this value within 1σ, supporting an LMC with a mass of at least 15% that of the Milky Way.

This measurement supports, and in some cases exacerbates, studies of the unusual nature of the Milky Way-LMC system. Dooley et al. (2017a) found a discrepancy between the predicted and observed population of LMC satellites. Our measurement of $M_{\rm LMC} \sim 1.8 \times 10^{11}\,M_{\odot}$ supports their predictions and further emphasizes the need for the continued study of the stellar mass function of satellites in the vicinity of the LMC. In addition, this measurement supports studies of the rarity of LMC mass satellites around Milky Way-like hosts (Busha et al. 2011), as well as predictions of the post-merger properties of the Milky Way and a massive LMC (Cautun et al. 2019). Furthermore, the LMC's impact on our sample of streams motivates the continued search for observational signs of its influence on other Milky Way structures (e.g., Belokurov et al. 2019; Conroy et al. 2021; Erkal et al. 2021; Ji et al. 2021; Petersen & Peñarrubia 2021).

5.1. Comparison to Previous Measurements

Prior to this work, two streams had been used to fit the mass of the LMC—OC (Erkal et al. 2019) and Sagittarius (Vasiliev et al. 2021). Erkal et al. (2019) measured an LMC mass of $1.38^{+0.27}_{-0.24} \times 10^{11}\,M_{\odot}$, and Vasiliev et al. (2021) obtained a consistent measurement of $M_{\rm LMC} = 1.3 \pm 0.3 \times 10^{11}\,M_{\odot}$.

As mentioned in Section 4.3, our fit to OC is a particularly interesting comparison to the results of fitting the same stream by Erkal et al. (2019). In this work, OC prefers an LMC mass of $18.8^{+4.0}_{-3.5} \times 10^{10}\,M_{\odot}$, which differs from the result of the Erkal et al. (2019) by $\sim 1\sigma$. This may be due in part to the fact that we are fitting a different data set, and in particular that Erkal et al. (2019) did not include radial velocities in their likelihood. In fact, the Erkal et al. (2019) best-fit model does not match the S^5 radial velocity measurements along the southern portion of the stream.

Another important distinction is that we do not fit the Milky Way potential, whereas Erkal et al. (2019) allow the mass, shape, and orientation of the Milky Way to vary; they find that the OC stream prefers a substantially asymmetric halo shape. Similarly, Vasiliev et al. (2021) find that the Sagittarius stream prefers a twisted dark matter halo that is aligned with the Milky Way disk in the inner halo but flattened in an almost

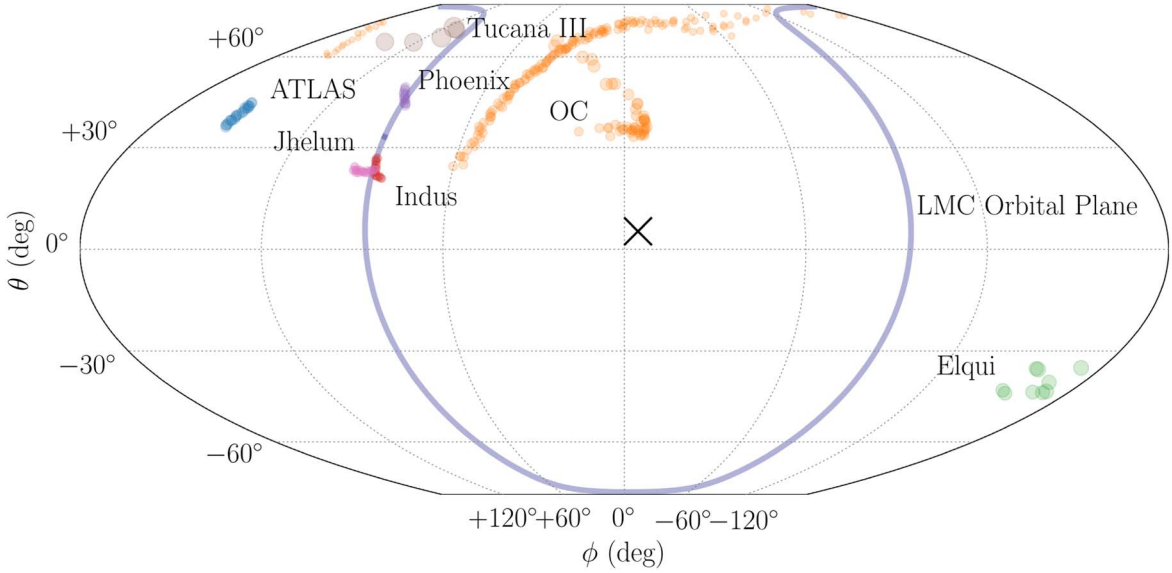

Figure 8. The position around the LMC at which each stream passes at closest approach. θ and ϕ represent the polar angles of the closest approach of each stream as viewed from the center of the LMC. The coordinate system is identical to Galactocentric coordinates shifted to the center of the LMC. The cross shows the direction of the LMC's orbital angular momentum and the blue line shows the plane of the LMC's orbit around the Milky Way. The points are spaced by 0.1° in ϕ_1 along the stream, and the size of the points is inversely proportional to the distance of closest approach to the LMC. Most of the streams pass to the north of the LMC, while Elqui passes below the galaxy. Each stream probes a different part of the LMC potential, by passing by at a different position, distance, and time. Ultimately, we will be able to use a large population of streams to constrain the disrupting, asymmetrical potential of the LMC.

perpendicular direction in the outskirts. This suggests that further work on simultaneously fitting multiple streams in a flexible joint Milky Way and LMC potential is necessary in order to entangle the complex interplay between the LMC and Milky Way potentials.

5.2. Shape of the LMC

The LMC is also known to have an asymmetric potential and in fact is disrupting as it orbits the Milky Way (e.g., Garavito-Camargo et al. 2019, 2021; Petersen & Peñarrubia 2020). In this work, we have used a simplified model of the LMC. We have modeled the potential of the LMC as a spherical Hernquist profile (Hernquist 1990), while in reality the LMC potential is more complex. A more realistic model of the LMC potential is necessary to explore the full complexity of the interactions between the LMC and Milky Way stellar streams. The fact that the LMC is a complex, nonspherical, disrupting system suggests that the S^5 streams may experience very different effects from the LMC depending on which part of the galaxy they pass by and at what time.

To explore this idea further, Figure 8 shows the predicted point of closest approach of each stream relative to the LMC. Each stream probes a different part of the LMC potential, and notably Elqui passes on the opposite side of the LMC from the other streams. In this figure we also show the orbital plane of the LMC around the Milky Way (blue line). Since the LMC material spreads out the most within this plane (e.g., see Figure 10 in Erkal et al. 2019), the streams closest to this plane likely experience a stronger LMC force field than those farther away. As we continue to build up our data set, our population of streams, and the complexity of our models, we should be able to use each of these streams to measure not only the total mass of the LMC, but its disrupting, asymmetrical radial profile.

6. Conclusions

The dynamical influence of the LMC on structures in the Milky Way has been the focus of much recent work (e.g., Erkal et al. 2018, 2019, 2021; Erkal & Belokurov 2020; Petersen & Peñarrubia 2020; Vasiliev et al. 2021). Here, we measure the LMC mass with five streams in the Southern Galactic hemisphere with full 6D phase-space measurements. These streams are sensitive to the LMC due to their proximity. Previous work has shown that many of these streams have proper motions misaligned with their stream tracks (Shipp et al. 2019), which is a telltale sign of a gravitational perturbation (e.g., Erkal et al. 2019). We find the mass of the LMC to be $\sim 1.8 \times 10^{11}\, M_\odot$, consistent with previous measurements of the LMC mass with stellar streams (Erkal et al. 2019; Vasiliev et al. 2021). By examining the interaction between each individual stream and the LMC, we can build a consistent picture of how the Milky Way's largest satellite has perturbed the population of stellar streams.

In order to understand the constraining power of each stream, we used a simple model which assumes the velocity kick imparted by the LMC is impulsive. We then decomposed the predicted velocity kicks into three directions relative to each stream's orbital plane: aligned with the angular momentum direction (i.e., perpendicular to the stream plane), in the radial direction (i.e., toward the Milky Way), and the tangential direction (i.e., along the stream). We found that the streams with the most stringent constraints on the LMC mass have significant velocity kicks that are perpendicular to the stream plane since these are visible as a misalignment between the proper motion direction and stream track.

Our best-fit models predict that several streams (Tuc III, Elqui, and Phoenix) are expected to have a significant misalignment along the line of sight. This alignment should be observable by comparing their distance gradient with the ratio of the radial velocity to the proper motion along the stream. These are currently not measurable due to the relatively

large uncertainty in distance compared to the other observables. With improved measurements of radial velocities and distance gradients in the future we should be able to more precisely measure the impact of the LMC in the radial direction. The detection of this misalignment will allow us to better constrain the LMC mass with these streams.

Although the main result of this work is that we can successfully model all of the streams with an LMC of mass $\sim 1.8 \times 10^{11} M_{\odot}$, there are a number of additional avenues for exploration. First, we have varied the LMC mass but we have kept the Milky Way fixed. Fitting these streams, along with streams from the Northern Galactic hemisphere, will likely provide strong constraints on the shape of the Milky Way's dark matter halo. Second, we have neglected the tidal deformation of the Milky Way and LMC, which may have a substantial effect on these streams. Interestingly, the streams considered in this work approach the LMC from a variety of directions (see Figure 8), suggesting that they will be a powerful probe of any deformations of the LMC.

Furthermore, in this work we fit the mass of the LMC with five of the stellar streams observed in the first year of S^5 observations. S^5 has now measured radial velocities of more than 20 stellar streams and observations are ongoing. In addition, future photometric surveys such as the Vera C. Rubin Observatory Legacy Survey of Space and Time (LSST) will observe more distant streams, many of which will have passed on the opposite side of the LMC (see Elqui in Figure 8), and will provide a more complete view of the potential of the LMC.

Further study of the complexity of the Milky Way and LMC potential with a large population of stellar streams will build upon this work to reveal a more complete picture of the effect of the Milky Way's largest satellite on our Galaxy.

We thank Paul McMillan for providing the MCMC chains from his analysis in McMillan 2017. This paper is based upon work that is supported by the Visiting Scholars Award Program of the Fermilab Universities Research Association. N.S. thanks the LSSTC Data Science Fellowship Program. T.S.L. is supported by NASA through Hubble Fellowship grant HF2-51439.001 awarded by the Space Telescope Science Institute, which is operated by the Association of Universities for Research in Astronomy, Inc., for NASA, under contract NAS5-26555. A.B.P. is supported by NSF grant AST-1813881. This research has been supported in part by the Australian Research Council Centre of Excellence for All Sky Astrophysics in 3 Dimensions (ASTRO 3D) through project number CE170100013. This paper includes data obtained with the AAT in Australia. We acknowledge the traditional owners of the land on which the AAT stands, the Gamilaraay people, and pay our respects to elders past and present. This work has made use of data from the European Space Agency (ESA) mission Gaia (https://www.cosmos.esa.int/gaia), processed by the Gaia Data Processing and Analysis Consortium (DPAC, https://www.cosmos.esa.int/web/gaia/dpac/consortium). Funding for the DPAC has been provided by national institutions, in particular the institutions participating in the Gaia Multilateral Agreement.

This project used public archival data from the DES. Funding for the DES Projects has been provided by the U.S. Department of Energy, the U.S. National Science Foundation, the Ministry of Science and Education of Spain, the Science and Technology Facilities Council of the United Kingdom, the Higher Education Funding Council for England, the National Center for Supercomputing Applications at the University of Illinois at Urbana-Champaign, the Kavli Institute of Cosmological Physics at the University of Chicago, the Center for Cosmology and Astro-Particle Physics at the Ohio State University, the Mitchell Institute for Fundamental Physics and Astronomy at Texas A&M University, Financiadora de Estudos e Projetos, Fundação Carlos Chagas Filho de Amparo à Pesquisa do Estado do Rio de Janeiro, Conselho Nacional de Desenvolvimento Científico e Tecnológico and the Ministério da Ciência, Tecnologia e Inovação, the Deutsche Forschungsgemeinschaft, and the Collaborating Institutions in the Dark Energy Survey. The Collaborating Institutions are Argonne National Laboratory, the University of California at Santa Cruz, the University of Cambridge, Centro de Investigaciones Energéticas, Medioambientales y Tecnológicas-Madrid, the University of Chicago, University College London, the DES-Brazil Consortium, the University of Edinburgh, the Eidgenössische Technische Hochschule (ETH) Zürich, Fermi National Accelerator Laboratory, the University of Illinois at Urbana-Champaign, the Institut de Ciències de l'Espai (IEEC/CSIC), the Institut de Física d'Altes Energies, Lawrence Berkeley National Laboratory, the Ludwig-Maximilians Universität München and the associated Excellence Cluster Universe, the University of Michigan, the National Optical Astronomy Observatory, the University of Nottingham, The Ohio State University, the OzDES Membership Consortium, the University of Pennsylvania, the University of Portsmouth, SLAC National Accelerator Laboratory, Stanford University, the University of Sussex, and Texas A&M University. Based in part on observations at Cerro Tololo Inter-American Observatory, National Optical Astronomy Observatory, which is operated by the Association of Universities for Research in Astronomy (AURA) under a cooperative agreement with the National Science Foundation.

Appendix A
Model Parameters

Table A1 lists the values of each parameter for the best-fit model to each stream, including stream progenitor and LMC parameters. Table A2 presents the orbital parameters (pericenter, apocenter, and the orientation of the orbital plane) for each stream. Table A3 includes the parameters of the Milky Way potential used in this work.

Table A1
Stream Progenitor and LMC Parameters

Parameter	ATLAS	OC	Elqui	Indus	Phoenix	Tucana III	Jhelum
$\phi_{2,\ \mathrm{prog}}$ (deg)	0.73	–0.77	0.31	0.30	−0.11	–0.10	0.01
$\sigma_{\phi 2,\ \mathrm{prog}}$ (deg)	0.30	⋯	0.18	0.48	0.11	0.07	0.29
$v_{r,\mathrm{prog}}$ (km s^{-1})	−110.09	96.97	−57.60	-52.83	47.61	−102.26	–5.35
$\sigma_{v_r,\mathrm{prog}}$ (km s^{-1})	4.06	⋯	13.60	4.83	3.14	0.89	18.41
d_{prog} (kpc)	21.22	18.78	52.85	15.77	17.29	23.97	12.79
$\mu_{\phi_1}\star$, prog (mas yr^{-1})	−0.40	4.25	−0.56	–5.74	−0.92	0.21	–7.13
μ_{ϕ_2}, prog (mas yr^{-1})	−0.90	1.95	−0.32	–1.27	−2.55	-1.60	–3.15
M_{LMC} ($10^{10}\,M_\odot$)	16.04	18.18	17.95	17.21	6.93	15.00	15.00
$v_{r,\mathrm{LMC}}$ (km s^{-1})	262.51	263.91	263.93	261.78	262.13	262.20	262.20
d_{LMC} (kpc)	49.48	51.36	48.44	50.19	50.05	49.97	49.97
$\mu_\alpha\star$, LMC (mas yr^{-1})	1.91	1.92	1.91	1.91	1.91	1.91	1.91
μ_δ, LMC (mas yr^{-1})	0.21	0.36	0.17	0.22	0.23	0.23	0.23
M_{prog} ($M_\odot$)	2×10^4	1×10^7	1×10^6	1×10^7	2×10^4	2×10^3	2×10^7
$r_{s,\mathrm{prog}}$ (kpc)	0.01	0.5	0.1	0.1	0.01	0.05	0.1

Note. Progenitor and LMC parameters for the best-fit stream models. Note that for Tucana III and Jhelum, all LMC parameters were fixed. For all streams, M_{prog} and $r_{\mathrm{s,prog}}$ were fixed. See parameter descriptions in Table 1.

Table A2
Stream Orbital Parameters

Parameter	ATLAS	OC	Elqui	Indus	Phoenix	Tucana III	Jhelum
r_{peri} (kpc)	$12.7^{+0.2}_{-0.2}$	$16.3^{+7.6}_{-0.1}$	$9.7^{+0.7}_{-0.9}$	$12.9^{+0.2}_{-0.1}$	$13.1^{+0.2}_{-0.2}$	$2.8^{+0.1}_{-0.1}$	$9.0^{+0.1}_{-0.2}$
r_{apo} (kpc)	$40.0^{+0.4}_{-0.4}$	$69.1^{+0.7}_{-0.8}$	$66.9^{+3.2}_{-2.2}$	$19.9^{+1.8}_{-1.0}$	$18.5^{+0.1}_{-0.1}$	$44.3^{+5.1}_{-0.7}$	$29.5^{+0.5}_{-1.8}$
ϕ (deg)	349.2	190.4	344.7	125.7	61.8	322.9	119.5
ψ (deg)	114.9	137.8	90.9	110.4	119.9	71.5	97.7

Note. Orbital parameters of the best-fit stream models. ϕ and ψ are the Galactocentric azimuthal and polar angles of the orbital pole, respectively.

Table A3
Potential Parameters

Parameter	Property		
$\Sigma_{0,\mathrm{thin}}$	679.3 $M_\odot$ pc^{-2}	v_0	233.7 km s^{-1}
$R_{d,\mathrm{thin}}$	2.823 kpc	M_b	$9.821\times10^9\,M_\odot$
$\Sigma_{0,\mathrm{thick}}$	231.8 $M_\odot$ pc^{-2}	$M_{d,\mathrm{thin}}$	$3.403\times10^{10}\,M_\odot$
$R_{d,\mathrm{thick}}$	2.956 kpc	$M_{d,\mathrm{thick}}$	$1.272\times10^{10}\,M_\odot$
$\rho_{0,b}$	104.7 $M_\odot$ pc^{-3}	M_{v}	$8.273\times10^{11}\,M_\odot$
$\rho_{0,h}$	0.01576 $M_\odot$ pc^{-3}	$c_{v'}$	15.07
r_h	13.14 kpc		
R_0	8.228 kpc		
U	8.406 km s^{-1}		
V	12.01 km s^{-1}		
W	7.280 km s^{-1}		

Note. Parameters of the potential from McMillan (2017), which we use to fit streams in this work. We note that the parameters here come from a realization of the posterior MCMC chains in McMillan (2017) and are thus consistent with that work. For ease of use, the parameters are in the same format as McMillan (2017).

Appendix B
Stream Models

Figures B1 and B2 show each of the stream models fit to the S5, DES, and Gaia data. The models are shown in blue, and the red points represent that data. For additional details, see Figure 1.

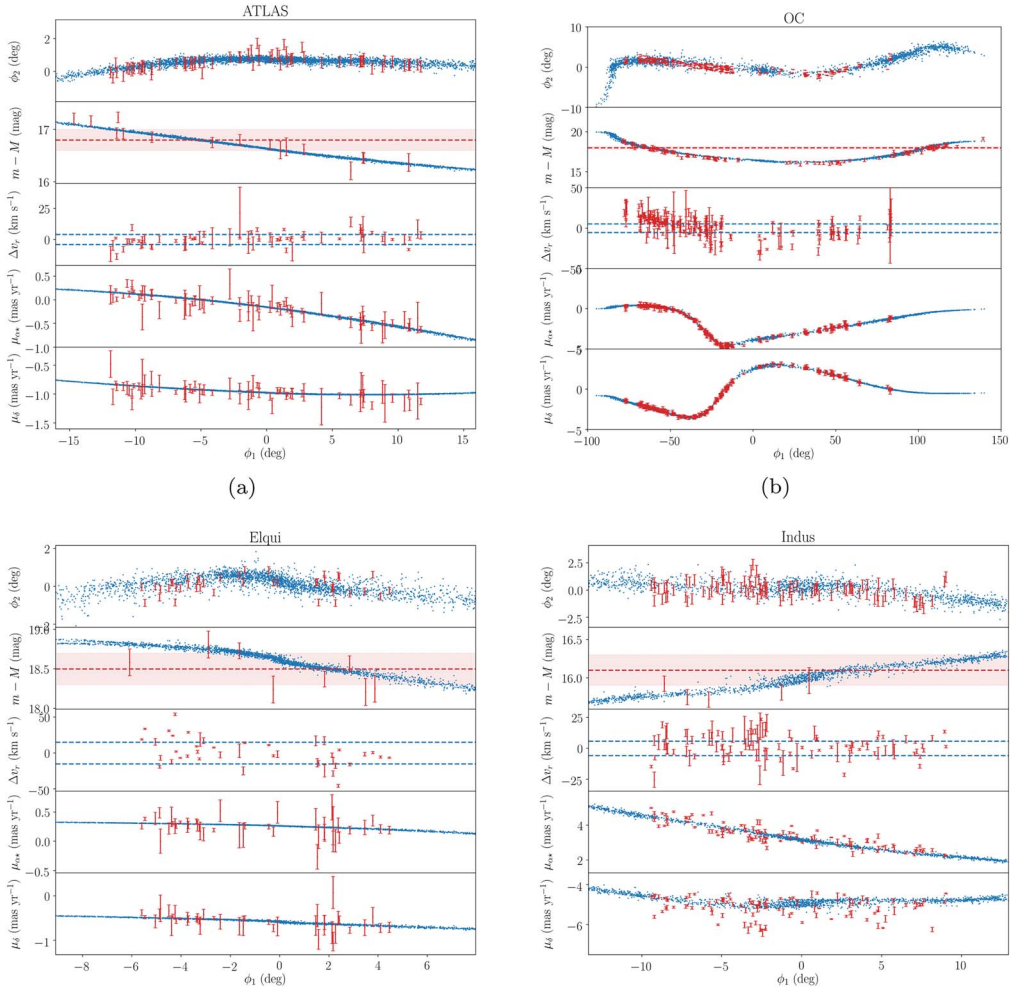

Figure B1. Stream models for (a) ATLAS, (b) OC, (c) Elqui, (d) Indus.

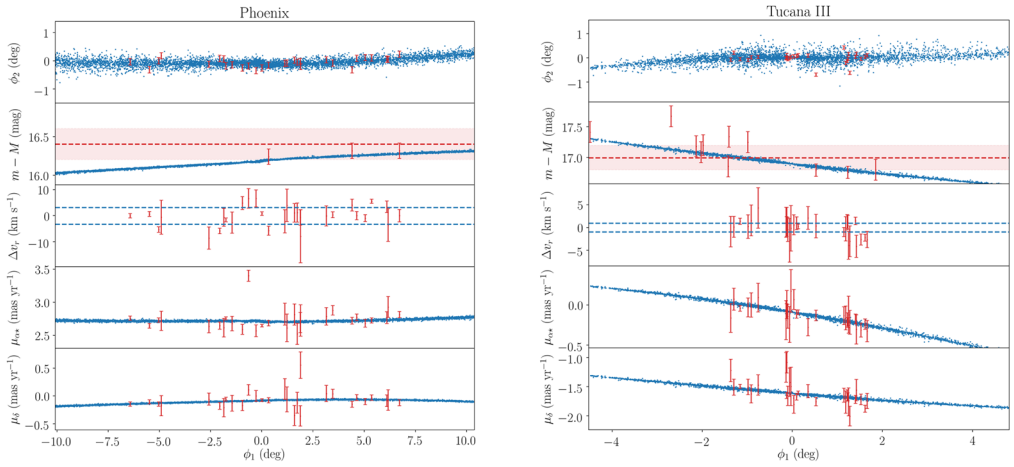

(e) (f)

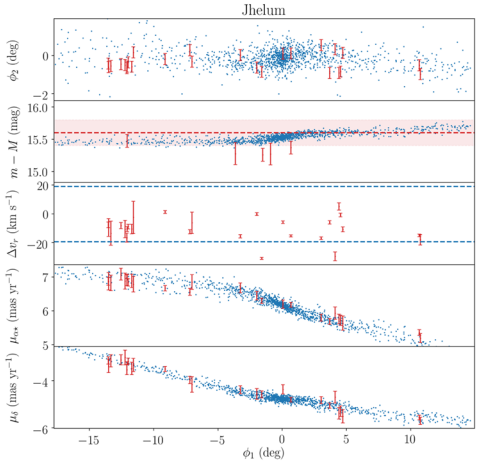

(g)

Figure B2. Stream models for (e) Phoenix, (f) Tucana III, and (g) Jhelum.

ORCID iDs

Nora Shipp https://orcid.org/0000-0003-2497-091X
Alex Drlica-Wagner https://orcid.org/0000-0001-8251-933X
Ting S. Li https://orcid.org/0000-0002-9110-6163
Andrew B. Pace https://orcid.org/0000-0002-6021-8760
Sergey E. Koposov https://orcid.org/0000-0003-2644-135X
Lara R. Cullinane https://orcid.org/0000-0001-8536-0547
Gary S. Da Costa https://orcid.org/0000-0001-7019-649X
Alexander P. Ji https://orcid.org/0000-0002-4863-8842
Kyler Kuehn https://orcid.org/0000-0003-0120-0808
Geraint F. Lewis https://orcid.org/0000-0003-3081-9319
Dougal Mackey https://orcid.org/0000-0002-6529-8093
Jeffrey D. Simpson https://orcid.org/0000-0002-8165-2507
Zhen Wan https://orcid.org/0000-0002-3105-3821
Daniel B. Zucker https://orcid.org/0000-0003-1124-8477
Joss Bland-Hawthorn https://orcid.org/0000-0001-7516-4016
Peter S. Ferguson https://orcid.org/0000-0001-6957-1627

References

Balbinot, E., Yanny, B., Li, T. S., et al. 2016, ApJ, 820, 58
Behroozi, P. S., Marchesini, D., Wechsler, R. H., et al. 2013, ApJ, 777, L10
Belokurov, V., Deason, A. J., Erkal, D., et al. 2019, MNRAS, 488, L47
Belokurov, V., & Koposov, S. E. 2016, MNRAS, 456, 602
Belokurov, V., Zucker, D. B., Evans, N. W., et al. 2006, ApJL, 642, L137
Besla, G., Kallivayalil, N., Hernquist, L., et al. 2007, ApJ, 668, 949
Bonaca, A., Conroy, C., Price-Whelan, A. M., & Hogg, D. W. 2019, ApJL, 881, L37
Boylan-Kolchin, M., Springel, V., White, S. D. M., & Jenkins, A. 2010, MNRAS, 406, 896
Busha, M. T., Wechsler, R. H., Behroozi, P. S., et al. 2011, ApJ, 743, 117
Cautun, M., Deason, A. J., Frenk, C. S., & McAlpine, S. 2019, MNRAS, 483, 2185
Clementini, G., Ripepi, V., Molinaro, R., et al. 2019, A&A, 622, A60
Conroy, C., Naidu, R. P., Garavito-Camargo, N., et al. 2021, Natur, 592, 534
Cullinane, L. R., Mackey, A. D., Da Costa, G. S., et al. 2020, MNRAS, 497, 3055
de Boer, T. J. L., Erkal, D., & Gieles, M. 2020, MNRAS, 494, 5315
Deason, A. J., Belokurov, V., & Evans, N. W. 2011, MNRAS, 416, 2903
Dehnen, W., & Binney, J. 1998, MNRAS, 294, 429
Dooley, G. A., Peter, A. H. G., Carlin, J. L., et al. 2017a, MNRAS, 472, 1060
Dooley, G. A., Peter, A. H. G., Yang, T., et al. 2017b, MNRAS, 471, 4894
Drlica-Wagner, A., Bechtol, K., Rykoff, E. S., et al. 2015, ApJ, 813, 109
Erkal, D., & Belokurov, V. 2015, MNRAS, 450, 1136
Erkal, D., Belokurov, V., Laporte, C. F. P., et al. 2019, MNRAS, 487, 2685
Erkal, D., & Belokurov, V. A. 2020, MNRAS, 495, 2554
Erkal, D., Deason, A. J., Belokurov, V., et al. 2021, MNRAS, 506, 2677
Erkal, D., Koposov, S. E., & Belokurov, V. 2017, MNRAS, 470, 60
Erkal, D., Li, T. S., Koposov, S. E., et al. 2018, MNRAS, 481, 3148
Fardal, M. A., van der Marel, R. P., Sohn, S. T., & del Pino Molina, A. 2019, MNRAS, 486, 936
Foreman-Mackey, D., Hogg, D. W., Lang, D., & Goodman, J. 2013, PASP, 125, 306
Gaia Collaboration, Brown, A. G. A., Vallenari, A., et al. 2018, A&A, 616, A1

Gaia Collaboration, Brown, A. G. A., Vallenari, A., et al. 2021, A&A, 649, A1
Gaia Collaboration, Prusti, T., de Bruijne, J. H. J., et al. 2016, A&A, 595, A1
Garavito-Camargo, N., Besla, G., Laporte, C. F. P., et al. 2019, ApJ, 884, 51
Garavito-Camargo, N., Besla, G., Laporte, C. F. P., et al. 2021, ApJ, 919, 109
Gibbons, S. L. J., Belokurov, V., & Evans, N. W. 2014, MNRAS, 445, 3788
Gómez, F. A., Besla, G., Carpintero, D. D., et al. 2015, ApJ, 802, 128
Grillmair, C. J. 2006, ApJL, 645, L37
Hernquist, L. 1990, ApJ, 356, 359
Holl, B., Audard, M., Nienartowicz, K., et al. 2018, A&A, 618, A30
Ibata, R. A., Lewis, G. F., & Martin, N. F. 2016, ApJ, 819, 1
Jethwa, P., Erkal, D., & Belokurov, V. 2016, MNRAS, 461, 2212
Ji, A. P., Koposov, S. E., Li, T. S., et al. 2021, ApJ, 921, 32
Ji, A. P., Li, T. S., Hansen, T. T., et al. 2020, AJ, 160, 181
Kallivayalil, N., van der Marel, R. P., Alcock, C., et al. 2006, ApJ, 638, 772
Kallivayalil, N., van der Marel, R. P., Besla, G., Anderson, J., & Alcock, C. 2013, ApJ, 764, 161
Koposov, S. E. 2019, RVSpecFit: Radial Velocity and Stellar Atmospheric Parameter Fitting, Astrophysics Source Code Library ascl:1907.013
Koposov, S. E., Belokurov, V., Li, T. S., et al. 2019, MNRAS, 485, 4726
Koposov, S. E., Irwin, M., Belokurov, V., et al. 2014, MNRAS, 442, L85
Koposov, S. E., Rix, H.-W., & Hogg, D. W. 2010, ApJ, 712, 260
Laporte, C. F. P., Gómez, F. A., Besla, G., Johnston, K. V., & Garavito-Camargo, N. 2018, MNRAS, 473, 1218
Law, D. R., & Majewski, S. R. 2010, ApJ, 714, 229
Levine, E. S., Blitz, L., & Heiles, C. 2006, ApJ, 643, 881
Lewis, I. J., Cannon, R. D., Taylor, K., et al. 2002, MNRAS, 333, 279
Li, T. S., Ji, A. P., Pace, A. B., et al. 2021b, arXiv:2110.06950
Li, T. S., Koposov, S. E., Erkal, D., et al. 2021a, ApJ, 911, 149
Li, T. S., Koposov, S. E., Zucker, D. B., et al. 2019, MNRAS, 490, 3508
Li, T. S., Simon, J. D., Kuehn, K., et al. 2018, ApJ, 866, 22
Majewski, S. R., Kunkel, W. E., Law, D. R., et al. 2004, AJ, 128, 245
Majewski, S. R., Schiavon, R. P., Frinchaboy, P. M., et al. 2017, AJ, 154, 94
McMillan, P. J. 2017, MNRAS, 465, 76
Miyamoto, M., & Nagai, R. 1975, PASJ, 27, 533
Moster, B. P., Naab, T., & White, S. D. M. 2013, MNRAS, 428, 3121
Muraveva, T., Delgado, H. E., Clementini, G., Sarro, L. M., & Garofalo, A. 2018, MNRAS, 481, 1195
Peñarrubia, J., Gómez, F. A., Besla, G., Erkal, D., & Ma, Y.-Z. 2016, MNRAS, 456, L54
Petersen, M. S., & Peñarrubia, J. 2020, MNRAS, 494, L11
Petersen, M. S., & Peñarrubia, J. 2021, NatAs, 5, 251
Pietrzyński, G., Graczyk, D., Gieren, W., et al. 2013, Natur, 495, 76
Plummer, H. C. 1911, MNRAS, 71, 460
Sanders, J. L., Smith, L., & Evans, N. W. 2019, MNRAS, 488, 4552
Schommer, R. A., Suntzeff, N. B., Olszewski, E. W., & Harris, H. C. 1992, AJ, 103, 447
Sesar, B., Bovy, J., Bernard, E. J., et al. 2015, ApJ, 809, 59
Sharp, R., Saunders, W., Smith, G., et al. 2006, Proc. SPIE, 6269, 62690G
Shipp, N., Drlica-Wagner, A., Balbinot, E., et al. 2018, ApJ, 862, 114
Shipp, N., Li, T. S., Pace, A. B., et al. 2019, ApJ, 885, 3
Tavangar, K., Ferguson, P., & Shipp, N. 2021, arXiv:2110.03703
van der Marel, R. P., Alves, D. R., Hardy, E., & Suntzeff, N. B. 2002, AJ, 124, 2639
van der Marel, R. P., & Kallivayalil, N. 2014, ApJ, 781, 121
Vasiliev, E. 2018, MNRAS, 481, L100
Vasiliev, E., Belokurov, V., & Erkal, D. 2021, MNRAS, 501, 2279
Vera-Ciro, C., & Helmi, A. 2013, ApJ, 773, L4
Wan, Z., Guglielmo, M., Lewis, G. F., Mackey, D., & Ibata, R. A. 2020a, MNRAS, 492, 782
Wan, Z., Lewis, G. F., Li, T. S., et al. 2020b, Natur, 583, 768
Weinberg, M. D. 1998, MNRAS, 299, 499
Weinberg, M. D., & Blitz, L. 2006, ApJL, 641, L33
Zhao, G., Zhao, Y.-H., Chu, Y.-Q., Jing, Y.-P., & Deng, L.-C. 2012, RAA, 12, 723